NANO LETTERS

pubs.acs.org/NanoLett Letter

High Accuracy Ultrafast Spatiotemporal Pump−Probe Measurement of Electrical Thermal Transport in Thin Film Gold

Mauricio Segovia and Xianfan Xu*

Cite This: https://doi.org/10.1021/acs.nanolett.1c02210 Read Online

ACCESS | Metrics & More | Article Recommendations | Supporting Information

ABSTRACT: A high resolution spatiotemporal ultrafast pump−probe system is developed to examine the interactions and transport phenomena between the electrical and the lattice thermal subsystems during ultrafast laser−matter interactions. This system incorporates an ultrafast pump−probe scheme with a stationary probe beam that interrogates the response to a spatial scanning pump beam, providing a full spatiotemporal mapping of a material's response due to an ultrafast pump excitation. The material's response, which is highly sensitive to its transport properties, is measured with a high spatial accuracy of up to ±10 nm and subpicosecond time resolution. Details of achieving this high spatial accuracy are described, and a study of the ultrafast transport processes in thin film gold is demonstrated. With the aid of transport and optical response models, the electrical thermal transport properties of gold and the electron−lattice coupling constant are simultaneously determined.

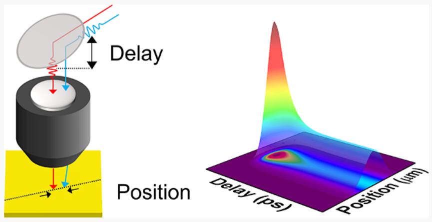

KEYWORDS: *ultrafast spatiotemporal measurements, electrical thermal conductivity, high resolution spatial mapping, ultrafast pump−probe measurements*

Ultrafast pump−probe experiments have been widely used for studying transport properties and understanding ultrafast light−matter interactions in advanced materials.[1−13] These ultrafast time-resolved experiments measure the optical response of a material after pump excitation with a temporal resolution on the order of the laser pulse duration. In the context of energy or thermal transport in metals or semiconductors, electrons in the irradiated material absorb the pump energy which causes a change in electron temperature. This temperature change leads to a change in the material's dielectric constant which dictates the optical response to the probe.[14] Pump−probe experiments with time scales longer than hundreds of picoseconds tend to provide information about a material as one thermodynamic system since energy carriers have thermalized and have reached local thermodynamic equilibrium with one another.[15,16] These experiments have long been used to extract the combined electron and lattice transport properties.

The electron and lattice subsystems of a solid both contribute to its thermal transport properties such as heat capacity and thermal conductivity. Differentiating the contributions of thermal transport from each subsystem is highly desirable for understanding the fundamentals of energy transport; however, it is not easily realized. Theoretically, numerically, and experimentally, ultrafast laser excitations have been studied within time scales shorter than ∼100 ps, where both subsystems are thermalized but not in equilibrium with one another.[17−20] In these works, the pump pulse optically excites the electron subsystem, forming a nonequilibrium state. This state quickly thermalizes within a few hundred femtoseconds to produce a Fermi−Dirac distribution of electron states with a definable temperature. Because these hot electrons have not had sufficient time to exchange energy with the lattice subsystem, the temperature difference between subsystems drives the exchange of thermal energy. These time-resolved experiments give rich information on the interaction of both subsystems and can be described by a two-temperature model (TTM).[21,22] However, these studies tend to focus on a spatially fixed response. The optical response mainly reflects the energy coupling between the electrons and the lattice, not the electron energy diffusion process that can provide its thermal transport properties.

To study the thermal transport process of the electron subsystem, spatial mapping of the electron thermal diffusion is needed. Since the electron−lattice nonequilibrium lasts for only a few picoseconds in most materials, this spatial mapping needs to be carried out with sufficiently fine time resolution before electron−lattice thermalization. Moreover, high spatial resolution is also needed to capture the small amount of diffusion that occurs within this time scale. Advances in instrumentation now allow for direct spatiotemporal measurement of the surface response of a material after laser excitation, providing more complete studies of materials such as semiconductors,[23−27] topological insulators,[28] and many

Received: June 6, 2021
Revised: August 17, 2021

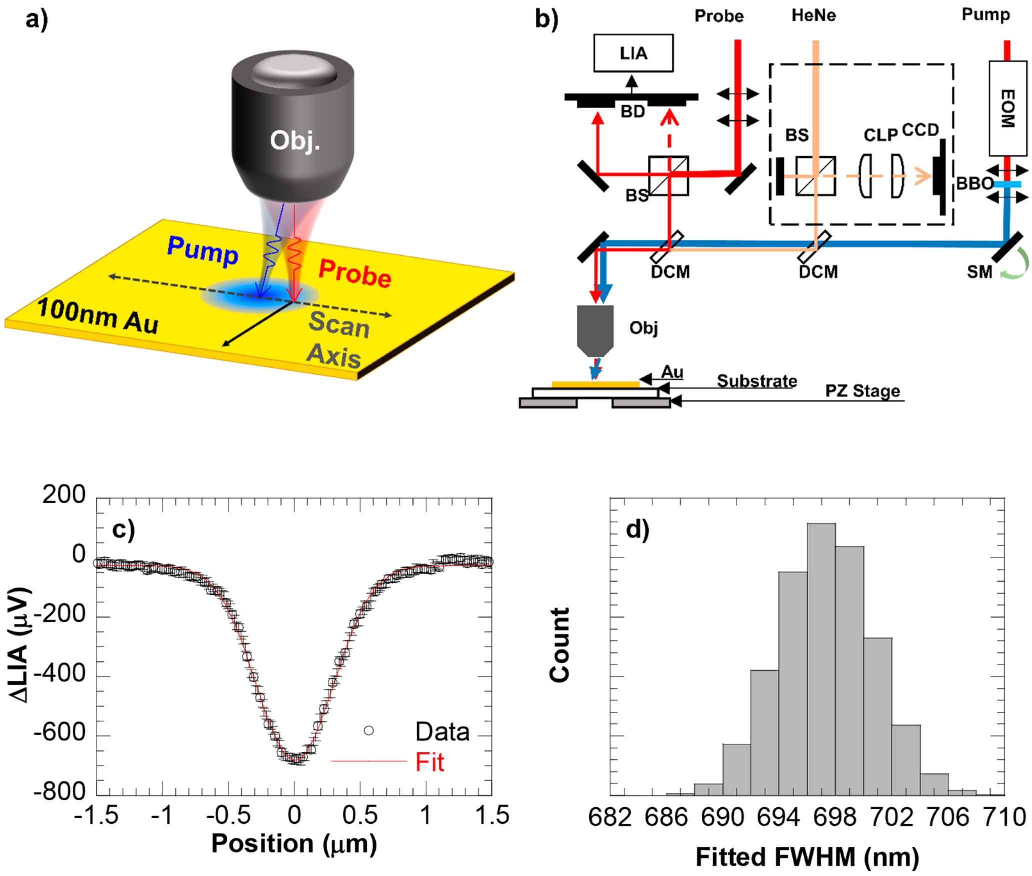

Figure 1. Experimental setup of an ultrafast spatiotemporal pump−probe measurement. (a) A close-up schematic of the experimental setup. In the experiment, the pump is moved along a line defined as the scan axis; the stationary probe interrogates the surface response to the pump. (b) An overview of the schematic of the experimental setup. An ultrafast laser output is split into a pump and a probe by a polarizing beam splitter (not shown). The probe is delayed by a mechanical stage (not shown) and split into a reference arm and a probe arm with the use of a beam splitter (BS) for balance detection (BD). The pump is modulated by an electro-optical modulator (EOM) and frequency doubled with the use of a barium borate crystal (BBO). Both the pump and the probe are focused on the surface of the thin gold film to near diffraction limited spot sizes. The reflected probe collection scheme utilizes a lock-in amplifier (LIA) and balance photodetector (BD). The pump position on the surface of the sample is controlled by a two-axis scanning mirror (SM). The relative distance between the surface of the sample and the objective is controlled by an autofocusing and autotracking system (dashed box) and a piezo stage. (c) A typical 1D cutline of a spatiotemporal measurement at 0 ps along with the best Gaussian fit. The error bars show the standard deviation of the probe signal as well as the position uncertainty, each quantified before each experiment. (d) A histogram of the fwhm from fitting a Gaussian function to each data set produced by a Monte Carlo analysis. The uncertainty of a given fwhm is defined as ±3 standard deviations away from the mean fwhm. In this example, this corresponds to a ±10 nm uncertainty for the measured 697 nm fwhm presented in (c).

others.[29,30] A recent work used spatiotemporal imaging to study the electron diffusion process with a spatial accuracy of 20 nm and a temporal resolution of 250 fs.[31] In this work, a high resolution spatiotemporal ultrafast pump−probe system is constructed, and its spatial accuracy is analyzed. A high spatial accuracy of ±10 nm is demonstrated, which allows for direct measurements of the electron contribution to thermal transport before thermalization with the lattice and electron−lattice coupling.

A schematic of the spatiotemporal pump−probe system is shown in Figure 1a,b. The system incorporates an ultrafast time-resolved pump−probe measurement scheme where the pump is scanned relative to the stationary probe under a microscope objective lens (Supporting Information Note 1).

The system also incorporates a home-built autofocusing/autotracking mechanism[32] to maintain the pump (507 nm fwhm) and probe (502 nm fwhm) at constant sizes at the surface, which is critical for this study. Briefly, a HeNe beam is brought into the shared beam path with a dichroic mirror. The reflected HeNe from the sample surface is sent to a pair of cylindrical lenses (CLP) and imaged onto a CCD. The dimensions of the HeNe are processed in real-time and are used as feedback to keep a fixed working distance between the surface and the objective (Supporting Information Note 2).

Accurate measurement of the relative position between the pump and probe is crucial to determine the spatial extent of electron thermal diffusion and to extract thermal properties. With the beam sizes maintained by the autofocusing/autotracking system, the accuracy of the relative position is mainly dependent on the positioning resolution and repeatability of the scanning mirror, which can perform repeatable nanometric displacement of the pump at the surface of the sample with 1.6 nm steps (Supporting Information Note 1). The overall accuracy of the spatial measurements is also influenced by the signal-to-noise ratio of the probe signal. Figure 1c,d illustrates how the overall accuracy (or uncertainty) of a spatial measurement is determined. A Gaussian function is used to fit the spatial pump−probe signal as seen in Figure 1c. The uncertainty analysis of a measured fwhm employs a Monte Carlo approach:

https://doi.org/10.1021/acs.nanolett.1c02210
Nano Lett. XXXX, XXX, XXX−XXX

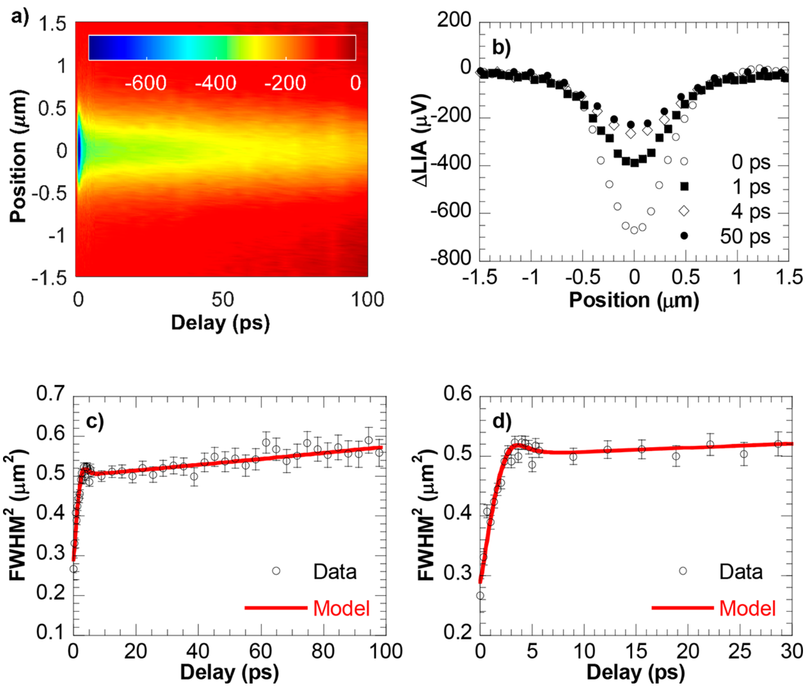

Figure 2. Experimental data of the spatial optical response. (a) A 2D colormap of the entire measurement results. The *z*-values are in units of μV from the lock-in amplifier. (b) Excerpts of the measured reflectance profile for 0, 1, 4, and 50 ps. (c) fwhm^2 of the calculated surface response to the 2.0 mJ/cm^2 pump interrogated by the probe from 0 to 100 ps along with the results of the numerical model. (d) fwhm^2 of the calculated surface response to the 2.0 mJ/cm^2 pump interrogated by the probe from 0 to 30 ps along with the results of the numerical model.

the uncertainty of the relative position between the pump and the probe and the uncertainty of the pump−probe signal are modeled by their respective cumulative density functions (CDFs). An inverse random sample is then taken from each CDF, and each data point in Figure 1c is modified to include these uncertainties to produce a new, simulated data set. A new fwhm is then extracted. This procedure is repeated 10 000 times, and a statistical distribution of the fitted fwhm values is obtained. Figure 1d shows the result of this analysis on the data set in Figure 1c, which indicates a fwhm of 679 ± 10 nm, with ±3 standard deviations defining the uncertainty of the fwhm measurement (Supporting Information Note 3).

There are multiple transport mechanisms in gold in which thermal energy is exchanged within and between subsystems such as electron ballistic motion, thermal diffusion, and coupling with the lattice as well as exchange with a substrate.[33−38] In this work, the heat transfer in the electron and lattice subsystems of gold and between gold and the substrate is modeled by a TTM:

$$C_e(T_e)\frac{\partial T_e}{\partial t} = \nabla\cdot(k_e(T_e, T_l)\nabla T_e) - G(T_e - T_l) + S \tag{1}$$

$$C_l\frac{\partial T_l}{\partial t} = \nabla\cdot(k_l\nabla T_l) + G(T_e - T_l) \tag{2}$$

$$C_s\frac{\partial T_s}{\partial t} = \nabla\cdot(k_s\nabla T_s) \tag{3}$$

Here, T_e/T_l and T_s denote the electron/lattice temperature of gold and the substrate temperature, respectively. The highest electron and lattice temperatures, calculated using the highest pulse energy in the experiments, are found to be far less than the Fermi temperature (64 000 K) and larger than the Debye temperature (180 K) of gold. Therefore, the electron heat capacity, C_e, is modeled by the Sommerfeld expansion.[39] The electron thermal conductivity, k_e, is derived from the Drude theory of metals.[39] The heat capacity and thermal conductivity of the lattice/substrate, C_l, k_l/C_s, and k_s, are taken as temperature independent due to low temperature rises. The heat transfer between subsystems is modeled through an electron−lattice coupling constant, G. Heat transfer between gold and the substrate is modeled as a thermal boundary conductance. The volumetric heat generation due to laser absorption is denoted as S, which includes effects from electron ballistic motion (Supporting Information Note 4).

For gold, a Drude−Lorentz model is typically used to describe its dielectric constant across a wide energy range.[40] However, because the probe center wavelength of 800 nm (1.55 eV) is well below the interband transition of gold (2.47 eV), the Drude theory of metals is used to model the optical response of the surface.[41,42]

$$\epsilon = \epsilon_\infty - \frac{{\omega_p}^2}{\omega(\omega + i\gamma_r(T_e, T_l))} \tag{4}$$

$$\gamma_r(T_e, T_l) = AT_e^2 + BT_l \tag{5}$$

Here, ϵ_∞ is the high frequency limit of the dielectric constant, ω_p is the plasma frequency, γ_r is the electron relaxation rate or damping constant as a function of T_e and T_s, ω is the optical frequency of the probe, and A and B are constants that will be discussed shortly. The plasma frequency is defined as ${\omega_p}^2 = ne^2/\epsilon_o m$, where n is the free electron density, e is the fundamental electron charge, ϵ_o is the free space permittivity, and m is the electron mass of gold. Clearly, ω_p depends on n which can change due to thermal excitation, optical excitation, and volumetric expansion. The change in n due to thermal excitation of *d*-band electrons has been found to be negligible

https://doi.org/10.1021/acs.nanolett.1c02210
Nano Lett. XXXX, XXX, XXX−XXX

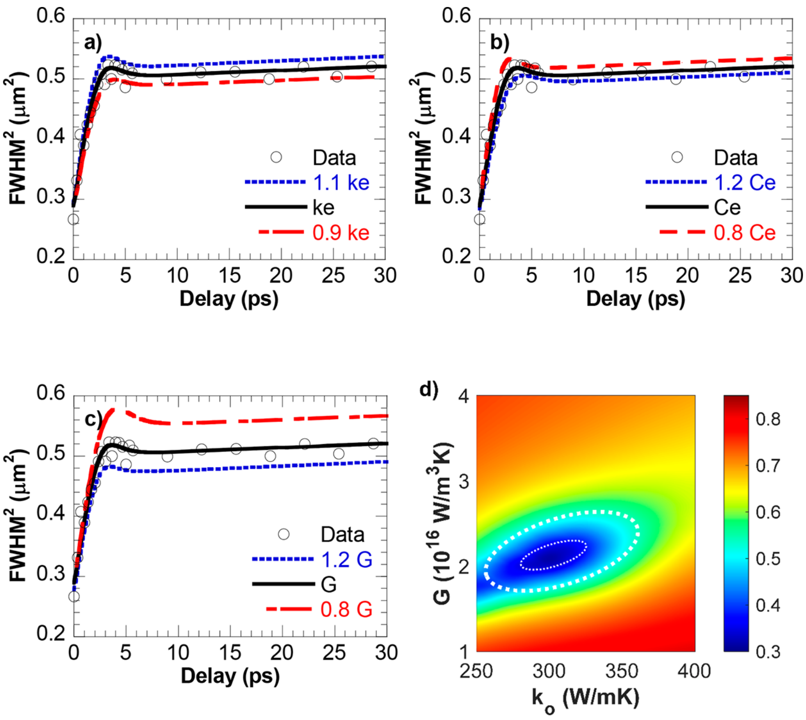

Figure 3. Measurements of thermophysical parameters. (a) Variation of the surface fwhm^2 versus electrical thermal conductivity. Here, $k_e = k_o T_e/T_l$, where k_o is the electron thermal conductivity at electron/lattice thermal equilibrium. (b) Variation of the surface fwhm^2 versus electrical heat capacity. Here, $C_e = \gamma T_e$ where γ is the linear coefficient in the electron heat capacity. (c) Variation of the surface fwhm^2 versus electron−lattice coupling constant. Error bars are removed for clarity. (d) A colormap of the root-mean-square error in units of μm^2 as a function k_o and G. The pair of parameters that gives the minimum root-mean-square error (0.30 μm^2) is found to be 315 W/(m K) and 2.1 × 10^{16} W/(m^3 K). The uncertainties of k_o and G are ±19% and ±18%, respectively, determined from the uncertainty in the fwhm^2 measurement (0.04 μm^2). The large, dashed ellipse illustrates the propagated uncertainty of the measurement uncertainty (shown by the small, dashed ellipse at a contour line of (0.30 + 0.04) μm^2).

within our temperature ranges.[43] For this work, the estimated effects of volumetric expansion and optical excitation are also found to be negligible (Supporting Information Note 4). Therefore, the main temperature dependence of the optical response lies in γ_r, the damping constant, which is written as a sum of temperature dependent collision frequencies: electron−electron scattering, calculated as AT_e^2, and electron−lattice scattering, calculated as BT_l.[14,39,44]

The key parameter of interest is the spatial extent of thermal diffusion. At a given delay time τ and a given pump/probe in-plane offset (Δx, Δy), the measured signal is considered as a weighted average of the spatial distribution of the surface response to the pump with respect to the probe intensity spatial distribution (Supporting Information Note 5). The weighted average of these two distributions gives an expression for the spatial/delay time dependency of the measured signal u_m.

$$u_m(\Delta x, \Delta y, \tau) = U_m(\tau) \exp\left[-\frac{\Delta x^2 + \Delta y^2}{\sigma_m^{\ 2}(\tau)}\right] \tag{6}$$

Along a center line, i.e., Δx or Δy set to 0, the surface response Gaussian width, σ_s, can be expressed as a function of the probe Gaussian width, σ_p, and the measured Gaussian width, σ_m.

$$\sigma_s^{\ 2}(\tau) = \sigma_m^{\ 2}(\tau) - \sigma_p^{\ 2} \tag{7}$$

In this work, $\sigma_m^{\ 2}$ and $\sigma_p^{\ 2}$ are measured and used to calculate $\sigma_s^{\ 2}$ using eq 7. The surface response is then modeled by solving eqs 1−3 for the temperature profiles and converted to a reflectance profile using eqs 4 and 5 and Fresnel equations. The uncertainty of σ_m from the Monte Carlo analysis and the uncertainty of σ_p deduced from a knife edge measurement are propagated to estimate the uncertainty in the surface response to the pump, σ_s, which is shown in the results below. Details of the propagated uncertainty in σ_s, and therefore $\sigma_s^{\ 2}$, are provided in Supporting Information Note 3.

Figure 2a shows the reflectance of the probe when the pump scans across the probe at delay times up to 100 ps after a 2.0 mJ/cm^2 pump pulse excitation. The negative values indicate that the reflectance signal drops first and then returns. The minimum signal value corresponds to the maximum electron temperature. From the data in Figure 2a, Gaussian curves of the measured reflectance signal at different delay times can be fitted and are shown in Figure 2b. The fwhm^2 of the surface response to the pump is calculated by using eq 7 where the measured fwhm^2 is subtracted by the probe fwhm^2, and the associated uncertainties are shown in Figure 2c as a function of delay time. It is seen that once the electron temperature has reached its maximum value within the laser pulse, there is a rapid rise in the fwhm^2 within the first ∼3 ps, followed by a gradual, monotonic rise after ∼8 ps. A numerical simulation of the surface response is also shown in Figure 2c for comparison. The electron thermal conductivity at thermal equilibrium, k_o, and electron−lattice coupling constant, G, are fitted simultaneously by a least-squares minimization routine. The best fitted results for k_o, 315 W/(m K), and G, 2.1 × 10^{16} W/(m^3 K), are used in the following simulation. The electron heat capacity used is $C_e = \gamma T_e$, where γ = 71 J/(m^3 K^2).[14] The lattice thermal

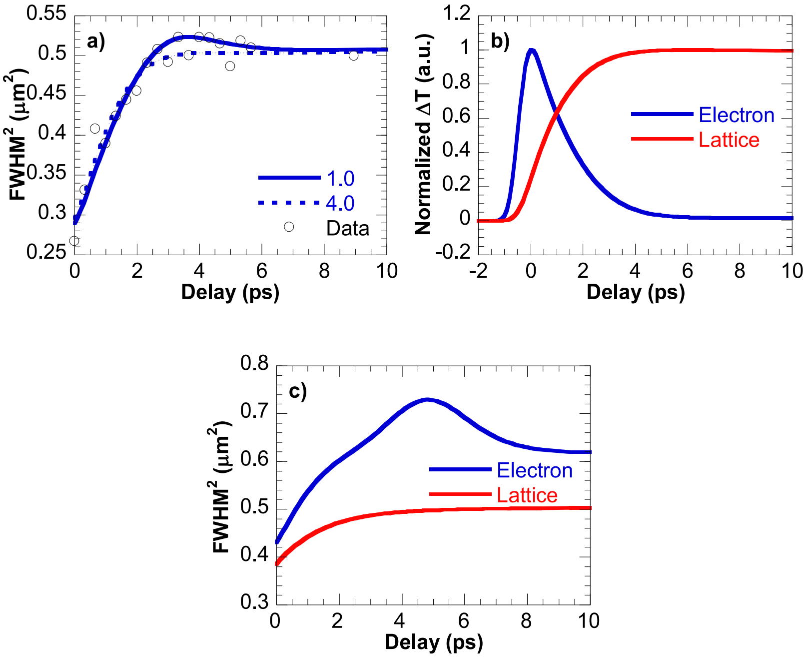

Figure 4. Effect of electron relaxation parameters on the fwhm^2 of the surface optical response. (a) The effect of electron–lattice scattering, BT_l, on the fwhm^2. The legend states the value of B in units of 10^{11} 1/(K s). Error bars in the experimental data are removed for clarity. (b) Electron and lattice subsystem temperatures, normalized to their respective maximum values, at the center of the pump as a function of the delay time. (c) fwhm^2 of the electron and lattice temperature as a function of the delay time. Here, the electron temperature profile has a hump due to the different thermal energy transport mechanisms in the center of the domain relative to the edges of the domain.

conductivity and heat capacity are fixed at 2.6 W/(m K) and 2.45×10^{16} J/(m^3 K), respectively.[14,45] All other thermophysical quantities are detailed in Supporting Information Note 4. There is close agreement between the experimental and the modeled results up to 100 ps, the longest delay time taken. At longer delays, there are larger fluctuations in fwhm^2, which are attributed to a weaker signal as well as a gradual loss of laser stability and laser power due to the long duration of the experiment (∼7 h). A slight hump in the signal near ∼4 ps appears in both the experimental and modeled results as seen in Figure 2d. The cause of this small hump will be discussed later.

The experimental data allows for extracting several important thermophysical parameters simultaneously. Measurement of the electrical thermal conductivity, k_e, separate from the lattice contribution, is of great interest. The simultaneous least-squares minimization routine produces a best fitted value of 315 W/(m K), which is in excellent agreement with literature values.[19,22,46,47] Figure 3a illustrates the sensitivity of the calculated surface response to ±10% variations of k_e. As k_e increases, a faster change in the fwhm^2 is observed; this is attributed to the increased electron diffusion length at early delay times. The electron heat capacity is usually well established if the density of states is known.[48−50] Therefore, a fit of C_e is not attempted. However, the sensitivity of the model to C_e is also explored numerically. Here, C_e is varied by ±20%, and the resulting sensitivity is shown in Figure 3b. As C_e decreases, a slower change in the fwhm^2 is observed compared with the experimental data. Comparing Figure 3a,b, changing k_e leads to a more pronounced change in the surface fwhm^2 when compared to C_e, implying a higher sensitivity to k_e.

The spatiotemporal measurement is also sensitive to the value of the electron–lattice coupling constant, G. Figure 3c shows that the transition time from a fast to slow rise of the fwhm^2 and the fwhm^2 value after this transition time are highly sensitive to G. A lower/higher value of G shifts the transition time to a longer/shorter delay time; this is because the electron–lattice thermalization time is proportional to $1/G$. From the experimental data, the best fitted value of G is determined to be 2.1×10^{16} W/(m^3 K) with the least-squares minimization routine. This value is well within the range of values found in literature: 1.0×10^{16} W/(m^3 K) to 4.0×10^{16} W/(m^3 K).[20,34,43,46,51−55]

The uncertainties of k_o and G are coupled due to the nature of the physical processes as well as the fitting routine. Qualitatively, this is shown in Figure 3d where the root-mean-square error (RMSE) is plotted as a function of both k_o and G. The best fitted k_o and G values give a minimum RMSE value of 0.30 μm^2. Once these values are established, the coupled uncertainties are calculated as a function of the fwhm^2 measurement uncertainty by applying the first-order principles of minimization.[56] A conservative, average fwhm^2 measurement uncertainty of 0.04 μm^2 (corresponding to a 30 nm uncertainty in a nominal 700 nm fwhm) across all data points, represented by the small, dashed ellipse in Figure 3d, is propagated in the uncertainty analysis. This results in propagated uncertainties of ±19% and ±18% for k_o and G, respectively, and is illustrated by the large, dashed ellipse in Figure 3d (Supporting Information Note 6).

In addition to the thermal properties of gold, the optical properties also play an important role in the measured optical response. Equation 5 gives the electron relaxation rate as a function of the electron and lattice temperatures, reflected in the values of A and B. A typically takes a consistent value of 1.2 $\times 10^7$ 1/(K^2 s) whereas B is found to vary between 1.0×10^{11} 1/(K s) and 4.0×10^{11} 1/(K s), depending on the method of estimation or measurement.[14,38,39,44,57,58] The variation of B is

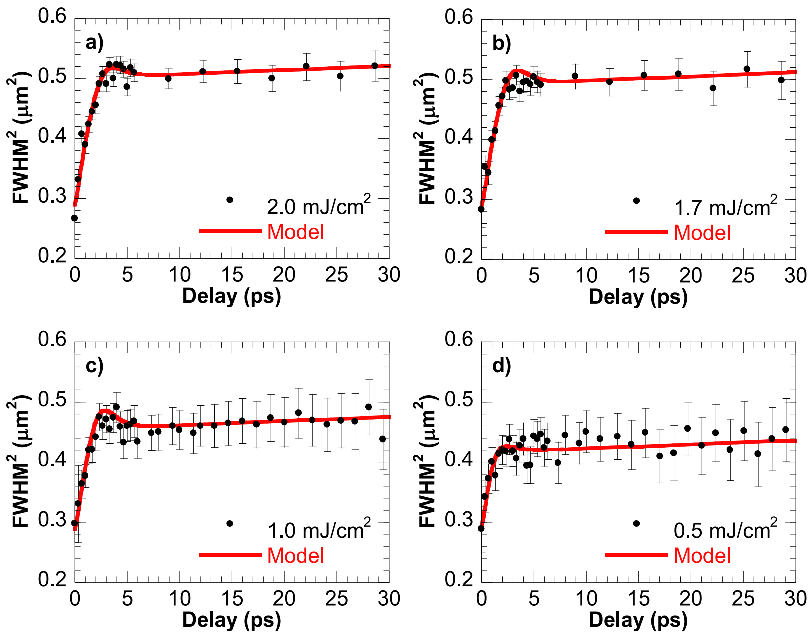

Figure 5. Optical response and modeling results at pump fluences of (a) 2.0 mJ/cm^2, (b) 1.7 mJ/cm^2, (c) 1.0 mJ/cm^2, and (d) 0.5 mJ/cm^2. For lower fluences, the overall signal strength is lower, and therefore, the error bars are larger.

explored numerically in Figure 4a. Here, a value of $B \approx 1.1 \times 10^{11}$ 1/(K s) captures the upper bound of a hump which appears clearly in the experimental fwhm^2 data around 4 ps. The data at the hump appears to have a large fluctuation; hence, B is not determined accurately, but its range shown in Figure 4a is well within literature values. Fortunately, the uncertainty in B does not affect the overall spatial extent of thermal diffusion before and after the appearance of the hump in Figure 4a, and therefore, it does not affect the sensitivity of the numerical model to thermal properties.

The origin of the hump lies in the temperature distributions of each subsystem. The temperature at the center of the pump and fwhm^2 of both the electron and lattice subsystems are shown in Figure 4b,c. The temperature changes are normalized to their respective maximum values for clarity: 1400 K for the electron subsystem and 315 K for the lattice subsystem at a pump fluence of 2.0 mJ/cm^2. From 0 to 4 ps, the transfer of thermal energy in electrons is dictated by electron−lattice coupling and thermal diffusion; the large increase in the fwhm^2 of the temperature profiles indicates that thermal diffusion is prominent. After 4 ps, once the subsystems are nearly thermalized, the electron fwhm^2 begins to decrease. Near the edge of the elevated temperature region, the temperatures of the electron and lattice subsystems converge, and the dominant process of thermal transport is diffusion within each subsystem. However, near the center, the contribution of electron−lattice coupling to the overall thermal transport in both systems is prominent but tends to decrease, causing a decrease in the fwhm^2 of the electron temperature distribution. The exact delay time occurrence of the hump in the optical response does not correspond to the exact delay time of the hump of the electron temperature distribution as the optical response is also a function of the lattice temperature, which has a fast rise in the first few picoseconds as shown in Figure 4c. Therefore, the hump in the optical response is caused by the transition from electron−lattice coupling and thermal diffusion to a mainly thermal diffusion process within each subsystem, especially the electron subsystem.

Pump fluence dependent measurements are conducted to test the fidelity of the measurements and computation results. Figure 5 shows the fwhm^2 of the surface response for four different fluences along with their corresponding modeling results using the same thermal properties and optical constant values as before. As the fluence of the incident pump beam is decreased, the overall signal-to-noise ratio is decreased, resulting in an increase in the fwhm^2 uncertainty. Nevertheless, the modeled results capture the fwhm^2 data for all the fluences.

In summary, a high spatial resolution ultrafast pump−probe system was developed to measure the spatial extent of transport processes from the nonequilibrated electron and lattice subsystems at early delay times to the fully thermalized system at later delay times. Due to the high spatial accuracy achieved, this system allowed for the direct measurement of transport properties. The electrical thermal conductivity and electron−lattice coupling constant are extracted from a TTM and optical response model with high sensitivity. The origin of the nonmonotonically increasing fwhm^2 of the optical response is explained by the spatially varying contribution to thermal transport in the electron subsystem due to electron−lattice coupling and thermal diffusion, which also allows an estimation of parameters in the optical model. Fluence dependent measurements were conducted and showed the fidelity of the experimental system and the numerical model.

■ ASSOCIATED CONTENT

Supporting Information

The Supporting Information is available free of charge at https://pubs.acs.org/doi/10.1021/acs.nanolett.1c02210.

(1) Optical system, laser spot size measurements, pump displacement calibration, and pulse characterization; (2) optical setup for autofocusing and autotracking; (3) fwhm measurement and uncertainty quantification; (4) effects of variations of thermophysical parameters used in the numerical model; (5) functional form of the surface response to the pump; and (6) simultaneous

https://doi.org/10.1021/acs.nanolett.1c02210
Nano Lett. XXXX, XXX, XXX−XXX

determination of parameters and their uncertainties (PDF)

AUTHOR INFORMATION

Corresponding Author

Xianfan Xu − *School of Mechanical Engineering and Birck Nanotechnology Center, Purdue University, West Lafayette, Indiana 47907, United States;* orcid.org/0000-0003-0580-4625; Email: xxu@ecn.purdue.edu

Author

Mauricio Segovia − *School of Mechanical Engineering and Birck Nanotechnology Center, Purdue University, West Lafayette, Indiana 47907, United States*

Complete contact information is available at:
https://pubs.acs.org/10.1021/acs.nanolett.1c02210

Author Contributions

X.X. conceived the concept of the work. M.S. developed the high spatial resolution ultrafast pump−probe system and performed the experiments and calculations. The manuscript is written by M.S. and X.X.

Notes

The authors declare no competing financial interest.

ACKNOWLEDGMENTS

Partial support of this work by the National Science Foundation (CBET-1804377, CBET-2051525) is gratefully acknowledged. The authors would like to thank Dr. Vasudevan Iyer, Shouyuan Huang, and Paul Somers for discussions.

REFERENCES

(1) Paddock, C. A.; Eesley, G. L. Transient Thermoreflectance from Thin Metal Films. *J. Appl. Phys.* **1986**, *60* (1), 285−290.

(2) Choi, G. M.; Min, B. C.; Lee, K. J.; Cahill, D. G. Spin Current Generated by Thermally Driven Ultrafast Demagnetization. *Nat. Commun.* **2014**, *5* (1), 1−8.

(3) Salihoglu, H.; Iyer, V.; Taniguchi, T.; Watanabe, K.; Ye, P. D.; Xu, X. Energy Transport by Radiation in Hyperbolic Material Comparable to Conduction. *Adv. Funct. Mater.* **2020**, *30* (6), 1905830.

(4) Zhang, D. L.; Zhu, J.; Qu, T.; Lattery, D. M.; Victora, R. H.; Wang, X.; Wang, J. P. High-Frequency Magnetoacoustic Resonance through Strain-Spin Coupling in Perpendicular Magnetic Multilayers. *Sci. Adv.* **2020**, *6* (38), No. eabb4607.

(5) Chen, K.; Song, B.; Ravichandran, N. K.; Zheng, Q.; Chen, X.; Lee, H.; Sun, H.; Li, S.; Gamage, G. A. G. U.; Tian, F.; Ding, Z.; Song, Q.; Rai, A.; Wu, H.; Koirala, P.; Schmidt, A. J.; Watanabe, K.; Lv, B.; Ren, Z.; Shi, L.; Cahill, D. G.; Taniguchi, T.; Broido, D.; Chen, G. Ultrahigh Thermal Conductivity in Isotope-Enriched Cubic Boron Nitride. *Science (Washington, DC, U. S.)* **2020**, *367* (6477), 555−559.

(6) Yoshida, S.; Aizawa, Y.; Wang, Z. H.; Oshima, R.; Mera, Y.; Matsuyama, E.; Oigawa, H.; Takeuchi, O.; Shigekawa, H. Probing Ultrafast Spin Dynamics with Optical Pump-Probe Scanning Tunnelling Microscopy. *Nat. Nanotechnol.* **2014**, *9* (8), 588−593.

(7) Jang, H.; Ryder, C. R.; Wood, J. D.; Hersam, M. C.; Cahill, D. G. 3D Anisotropic Thermal Conductivity of Exfoliated Rhenium Disulfide. *Adv. Mater.* **2017**, *29* (35), 1700650.

(8) Tian, F.; Song, B.; Chen, X.; Ravichandran, N. K.; Lv, Y.; Chen, K.; Sullivan, S.; Kim, J.; Zhou, Y.; Liu, T. H.; Goni, M.; Ding, Z.; Sun, J.; Gamage, G. A. G. U.; Sun, H.; Ziyaee, H.; Huyan, S.; Deng, L.; Zhou, J.; Schmidt, A. J.; Chen, S.; Chu, C. W.; Huang, P. Y.; Broido, D.; Shi, L.; Chen, G.; Ren, Z. Unusual High Thermal Conductivity in Boron Arsenide Bulk Crystals. *Science (Washington, DC, U. S.)* **2018**, *361* (6402), 582−585.

(9) Iyer, V.; Chen, Y. P.; Xu, X. Ultrafast Surface State Spin-Carrier Dynamics in the Topological Insulator Bi2Te2Se. *Phys. Rev. Lett.* **2018**, *121* (2), 026807.

(10) Miao, X.; Zhang, G.; Wang, F.; Yan, H.; Ji, M. Layer-Dependent Ultrafast Carrier and Coherent Phonon Dynamics in Black Phosphorus. *Nano Lett.* **2018**, *18* (5), 3053−3059.

(11) Iyer, V.; Segovia, M.; Wang, Y.; Wu, W.; Ye, P.; Xu, X. Infrared Ultrafast Spectroscopy of Solution-Grown Thin Film Tellurium. *Phys. Rev. B: Condens. Matter Mater. Phys.* **2019**, *100* (7), 075436.

(12) Huang, S.; Segovia, M.; Yang, X.; Koh, Y. R.; Wang, Y.; Ye, P. D.; Wu, W.; Shakouri, A.; Ruan, X.; Xu, X. Anisotropic Thermal Conductivity in 2D Tellurium. *2D Mater.* **2020**, *7* (1), 015008.

(13) Zhou, J.; Shin, H. D.; Chen, K.; Song, B.; Duncan, R. A.; Xu, Q.; Maznev, A. A.; Nelson, K. A.; Chen, G. Direct Observation of Large Electron−Phonon Interaction Effect on Phonon Heat Transport. *Nat. Commun.* **2020**, *11* (1), 1−9.

(14) Kittel, C. *Introduction to Solid State Physics*, 8th ed.; Wiley: New York, 2005.

(15) Cahill, D. G. Analysis of Heat Flow in Layered Structures for Time-Domain Thermoreflectance. *Rev. Sci. Instrum.* **2004**, *75* (12), 5119−5122.

(16) Schmidt, A. J.; Chen, X.; Chen, G. Pulse Accumulation, Radial Heat Conduction, and Anisotropic Thermal Conductivity in Pump-Probe Transient Thermoreflectance. *Rev. Sci. Instrum.* **2008**, *79* (11), 114902.

(17) Fann, W. S.; Storz, R.; Tom, H. W. K.; Bokor, J. Electron Thermalization in Gold. *Phys. Rev. B: Condens. Matter Mater. Phys.* **1992**, *46* (20), 13592−13595.

(18) Sun, C. K.; Vallée, F.; Acioli, L.; Ippen, E. P.; Fujimoto, J. G. Femtosecond Investigation of Electron Thermalization in Gold. *Phys. Rev. B: Condens. Matter Mater. Phys.* **1993**, *48* (16), 12365−12368.

(19) Bonn, M.; Denzler, D. N.; Funk, S.; Wolf, M.; Wellershoff, S.-S.; Hohlfeld, J. Ultrafast Electron Dynamics at Metal Surfaces: Competition between Electron-Phonon Coupling and Hot-Electron Transport. *Phys. Rev. B: Condens. Matter Mater. Phys.* **2000**, *61* (2), 1101−1105.

(20) Guo, L.; Xu, X. Ultrafast Spectroscopy of Electron-Phonon Coupling in Gold. *J. Heat Transfer* **2014**, *136* (12), 122401 DOI: 10.1115/1.4028543.

(21) Anisimov, S. I.; Kapeliovich, B. L.; Perel'man, T. L. Electron Emission from Metal Surfaces Exposed to Ultrashort Laser Pulses. *Sov. Phys. JEPT* **1975**, *39* (2), 375−377.

(22) Fann, W. S.; Storz, R.; Tom, H. W. K.; Bokor, J. Direct Measurement of Nonequilibrium Electron-Energy Distributions in Subpicosecond Laser-Heated Gold Films. *Phys. Rev. Lett.* **1992**, *68* (18), 2834−2837.

(23) Smith, L. M.; Wake, D. R.; Wolfe, J. P.; Levi, D.; Klein, M. V.; Klem, J.; Henderson, T.; Morkoç, H. Picosecond Imaging of Photoexcited Carriers in Quantum Wells: Anomalous Lateral Confinement at High Densities. *Phys. Rev. B: Condens. Matter Mater. Phys.* **1988**, *38* (8), 5788−5791.

(24) Ruzicka, B. A.; Werake, L. K.; Samassekou, H.; Zhao, H. Ambipolar Diffusion of Photoexcited Carriers in Bulk GaAs. *Appl. Phys. Lett.* **2010**, *97* (26), 262119.

(25) Gabriel, M. M.; Kirschbrown, J. R.; Christesen, J. D.; Pinion, C. W.; Zigler, D. F.; Grumstrup, E. M.; Mehl, B. P.; Cating, E. E. M.; Cahoon, J. F.; Papanikolas, J. M. Direct Imaging of Free Carrier and Trap Carrier Motion in Silicon Nanowires by Spatially-Separated Femtosecond Pump-Probe Microscopy. *Nano Lett.* **2013**, *13* (3), 1336−1340.

(26) Cating, E. E. M.; Pinion, C. W.; Van Goethem, E. M.; Gabriel, M. M.; Cahoon, J. F.; Papanikolas, J. M. Imaging Spatial Variations in the Dissipation and Transport of Thermal Energy within Individual Silicon Nanowires Using Ultrafast Microscopy. *Nano Lett.* **2016**, *16* (1), 434−439.

(27) Cating, E. E. M.; Pinion, C. W.; Christesen, J. D.; Christie, C. A.; Grumstrup, E. M.; Cahoon, J. F.; Papanikolas, J. M. Probing Intrawire, Interwire, and Diameter-Dependent Variations in Silicon

Nanowire Surface Trap Density with Pump-Probe Microscopy. *Nano Lett.* **2017**, *17* (10), 5956−5961.
(28) Kumar, N.; Ruzicka, B. A.; Butch, N. P.; Syers, P.; Kirshenbaum, K.; Paglione, J.; Zhao, H. Spatially Resolved Femtosecond Pump-Probe Study of Topological Insulator Bi 2 Se 3. *Phys. Rev. B: Condens. Matter Mater. Phys.* **2011**, *83*, 235306.
(29) Yoon, S. J.; Guo, Z.; Dos Santos Claro, P. C.; Shevchenko, E. V.; Huang, L. Direct Imaging of Long-Range Exciton Transport in Quantum Dot Superlattices by Ultrafast Microscopy. *ACS Nano* **2016**, *10* (7), 7208−7215.
(30) Deng, S.; Shi, E.; Yuan, L.; Jin, L.; Dou, L.; Huang, L. Long-Range Exciton Transport and Slow Annihilation in Two-Dimensional Hybrid Perovskites. *Nat. Commun.* **2020**, *11* (1), 1−8.
(31) Block, A.; Liebel, M.; Yu, R.; Spector, M.; Sivan, Y.; García De Abajo, F. J.; Van Hulst, N. F. Tracking Ultrafast Hot-Electron Diffusion in Space and Time by Ultrafast Thermomodulation Microscopy. *Sci. Adv.* **2019**, *5* (5), No. eaav8965.
(32) Bai, Z.; Wei, J. Focusing Error Detection Based on Astigmatic Method with a Double Cylindrical Lens Group. *Opt. Laser Technol.* **2018**, *106*, 145−151.
(33) Kaganov, M. I.; Lifshitz, I. M.; Tanatarov, L. V. Relaxation Between Electrons and the Crystalline Lattice. *Sov. Phys. JEPT* **1957**, *4* (2), 173−178.
(34) Allen, P. B. Theory of Thermal Relaxation of Electrons in Metals. *Phys. Rev. Lett.* **1987**, *59* (13), 1460−1463.
(35) Brorson, S. D.; Fujimoto, J. G.; Ippen, E. P. Femtosecond Electronic Heat-Transport Dynamics in Thin Gold Films. *Phys. Rev. Lett.* **1987**, *59* (17), 1962−1965.
(36) Qiu, T. Q.; Tien, C. L. Heat Transfer Mechanisms during Short-Pulse Laser Heating of Metals. *J. Heat Transfer* **1993**, *115* (4), 835−841.
(37) Chowdhury, I. H.; Xu, X. Heat Transfer in Femtosecond Laser Processing of Metal. *Numer. Heat Transfer, Part A* **2003**, *44* (3), 219−232.
(38) Guo, L.; Hodson, S. L.; Fisher, T. S.; Xu, X. Heat Transfer across Metal-Dielectric Interfaces during Ultrafast-Laser Heating. *J. Heat Transfer* **2012**, *134* (4), 042402 DOI: 10.1115/1.4005255.
(39) Ashcroft, N. W.; Mermin, N. D. *Solid State Physics*; Holt, Rinehart, and Winston: New York, 1976.
(40) Sehmi, H. S.; Langbein, W.; Muljarov, E. A. Optimizing the Drude-Lorentz Model for Material Permittivity: Method, Program, and Examples for Gold, Silver, and Copper. *Phys. Rev. B: Condens. Matter Mater. Phys.* **2017**, *95* (11), 115444.
(41) Johnson, P. B.; Christy, R. W. Optical Constants of the Noble Metals. *Phys. Rev. B* **1972**, *6* (12), 4370−4379.
(42) Derkachova, A.; Kolwas, K.; Demchenko, I. Dielectric Function for Gold in Plasmonics Applications: Size Dependence of Plasmon Resonance Frequencies and Damping Rates for Nanospheres. *Plasmonics* **2016**, *11* (3), 941−951.
(43) Lin, Z.; Zhigilei, L. V. Thermal Excitation of d Band Electrons in Au: Implications for Laser-Induced Phase Transformations. In *High-Power Laser Ablation VI*; Phipps, C. R., Ed.; SPIE: 2006; Vol. *6261*, p 62610U, DOI: 10.1117/12.674636.
(44) Anisimov, S. I.; Rethfeld, B. On the Theory of Ultrashort Laser Pulse Interaction with a Metal. In *Nonresonant Laser-Matter Interaction (NLMI-9)*; Konov, V. I., Libenson, M. N., Eds.; International Society for Optics and Photonics, 1997; Vol. *3093*, pp 192−203, DOI: 10.1117/12.271674.
(45) Wang, Y.; Lu, Z.; Ruan, X. First Principles Calculation of Lattice Thermal Conductivity of Metals Considering Phonon-Phonon and Phonon-Electron Scattering. *J. Appl. Phys.* **2016**, *119* (22), 225109.
(46) Wang, X. Y.; Riffe, D. M.; Lee, Y. S.; Downer, M. C. Time-Resolved Electron-Temperature Measurement in a Highly Excited Gold Target Using Femtosecond Thermionic Emission. *Phys. Rev. B: Condens. Matter Mater. Phys.* **1994**, *50* (11), 8016−8019.
(47) Du, G.; Yang, Q.; Chen, F.; Si, J.; Hou, X. Insight into the Thermionic Emission Regimes under Gold Film Thermal Relaxation Excited by a Femtosecond Pulse. *Appl. Surf. Sci.* **2011**, *257* (21), 9177−9182.
(48) Lee, S. J.; Chang Jeon, H.; Won Kang, T.; Souma, S. Transitions of Density of States and Heat Capacity in Spherical Quantum Structure Formed by a Thin Barrier. *Phys. E* **2008**, *40* (6), 2198−2200.
(49) Roslee, A. E.; Muzakir, S. K.; Ismail, J.; Yusoff, M. M.; Jose, R. A Heat Capacity Model of T3/2 Dependence for Quantum Dots. *Phys. Chem. Chem. Phys.* **2017**, *19* (1), 408.
(50) Gupta, A.; Verma, S. K.; Kumari, A.; Indu, B. D. Study of Electron Density of States and Electronic Heat Capacity of High-Temperature Cuprate Superconductor: L a 2−x S Rx C u O 4. *J. Supercond. Novel Magn.* **2020**, *33* (8), 2293−2297.
(51) Brorson, S. D.; Kazeroonian, A.; Moodera, J. S.; Face, D. W.; Cheng, T. K.; Ippen, E. P.; Dresselhaus, M. S.; Dresselhaus, G. Femtosecond Room-Temperature Measurement of the Electron-Phonon Coupling Constant in Metallic Superconductors. *Phys. Rev. Lett.* **1990**, *64* (18), 2172−2175.
(52) Qiu, T. Q.; Tien, C. L. Size Effects on Nonequilibrium Laser Heating of Metal Films. *J. Heat Transfer* **1993**, *115* (4), 842−847.
(53) Hohlfeld, J.; Wellershoff, S. S.; Güdde, J.; Conrad, U.; Jähnke, V.; Matthias, E. Electron and Lattice Dynamics Following Optical Excitation of Metals. *Chem. Phys.* **2000**, *251* (1−3), 237−258.
(54) Smith, A. N.; Norris, P. M. Influence of Intraband Transitions on the Electron Thermoreflectance Response of Metals. *Appl. Phys. Lett.* **2001**, *78* (9), 1240−1242.
(55) Lee, J. B.; Kang, K.; Lee, S. H. Comparison of Theoretical Models of Electron-Phonon Coupling in Thin Gold Films Irradiated by Femtosecond Pulse Lasers. *Mater. Trans.* **2011**, *52* (3), 547−553.
(56) Seber, G.; Wild, C. *Nonlinear Regression*; John Wiley and Sons Inc.: 2003.
(57) Van Vucht, R. J. M.; Van Kempen, H.; Wyder, P. Simple Transport Properties of Simple Metals: Classical Theories and Modern Experiments. *Rep. Prog. Phys.* **1985**, *48*, 853−905.
(58) Radue, E. L.; Tomko, J. A.; Giri, A.; Braun, J. L.; Zhou, X.; Prezhdo, O. V.; Runnerstrom, E. L.; Maria, J. P.; Hopkins, P. E. Hot Electron Thermoreflectance Coefficient of Gold during Electron-Phonon Nonequilibrium. *ACS Photonics* **2018**, *5* (12), 4880−4887.